Solar Physics
DOI: 10.1007/•••••-•••-•••-••••-•

Signatures of the slow solar wind streams from active regions in the inner corona

V. Slemzin[1] · L. Harra[2] · A. Urnov[1]
S. Kuzin[1] F. Goryaev[1,3] D. Berghmans[3]

Abstract The quasi-stationary solar wind is likely originated from many sources spatially distributed over the Sun. Some of local sources of the slow wind can be associated with plasma outflows at edges of active regions (ARs) detected spectroscopically. The EUV telescopes SPIRIT onboard *CORONAS-F*, TESIS onboard *CORONAS/Photon* and SWAP onboard *PROBA2* observed extended ray-like structures seen at the limb above active regions in ∼1 MK iron emission lines and described as "coronal rays". To verify the assumption that coronal rays represent signatures of plasma outflows we analyze an isolated AR observed by TESIS, EIS and XRT onboard *Hinode* as well as SECCHI/EUVI telescopes onboard *STEREO* A and B in the end of July - beginning of August 2009. During this period the initially closed structure of the AR has been evolved which resulted in appearance of coronal rays at the western limb. On August 1 EIS revealed two regions of outflows in the eastern and western sides of the AR with velocities V = 10–30 km s^{-1} accompanied with fan loops diverging from their boundaries. The Potential Field Source Surface model showed the open magnetic field configuration in the western outflow region adjacent to small coronal hole. Using the Differential Emission Measure analysis it was found that both outflow regions and fan loops had similar dominating components of plasma with temperature $T \approx$ 1 MK which was also responsible for the emission of coronal rays. We analyze properties of the outflows and their probable coronal signatures as well as supposed correlation between evolution of the AR and variation of parameters of the solar wind measured by *STEREO-B*, *ACE*, *WIND*, *STEREO-A*. The results of the study support the assumption that coronal rays are linked with outflows from ARs.

[1] P.N. Lebedev Physical Institute, Leninsky Pr., 53, Moscow, 119991, Russia. email: slem@sci.lebedev.ru
[2] UCL-Mullard Space Science Laboratory, Holmbury St Mary, Dorking, Surrey, RH5 6NT, UK. email: lkh@mssl.ucl.ac.uk
[3] Royal Observatory of Belgium, Ringlaan 3, 1180 Brussels, Belgium. email: david.berghmans@oma.be

1. Introduction

Since the discovery of the solar wind, the detection of its sources became one of the main fundamental problems of solar physics. It is believed that the quasi-stationary solar wind has two main components – the fast solar wind dominating at solar minimum, and the slow solar wind dominating at solar maximum. Early studies of the X-ray solar images on *Skylab* (Levine *et al.*, 1977) and later measurements of the solar wind with *Ulysses* (Gosling *et al.*, 1995) and *ACE* (McComas *et al.*, 2001) have shown that the fast solar wind at the solar maximum originates from polar coronal holes (PCH). Analysis of *Ulysses* and *ACE* data have shown that in different phases of the solar cycle the slow wind emanates from various local source regions **which may be attributed** to boundaries of PCH and equatorial coronal holes (ECH) (Neugebauer *et al.*, 1998; Neugebauer *et al.*, 2002; Liewer, Neugebauer, and Zurbuchen, 2003; Wang, Ko, and Grappin, 2009), **non-coronal hole sources (**Zhao, Zurbuchen, and Fisk, 2009**)**, helmet streamers (Sheeley *et al.*, 1997) and active regions (ARs) (Hefti *et al.*, 2000; Liewer *et al.*, 2001; Liewer, Neugebauer, and Zurbuchen, 2004). In general, **sources of the slow solar wind are not sufficiently investigated for reliable theoretical modeling of the slow solar wind.**

The source regions of the quasi-stationary solar wind are ordinarily identified from the solar wind data measured near the Earth using two complementary methods. The first is the ballistic back-tracking method described firstly by Nolte and Roelof (1973) and developed further in the more sophisticated Wang-Sheeley-Arge (WSA) model (Wang and Sheeley, 1990). The back-tracking method is based on two main assumptions: (1) the solar wind moves between the solar surface and so-called "source surface" (SS) typically at $R = 2.5R_{\rm sun}$ along divergent commonly non-radial open magnetic field lines; (2) between the SS and the Earth it propagates along radial open magnetic field lines with constant speed equal to its value measured near the Earth. The magnetic field in the inner corona is usually extrapolated on the basis of synoptic maps of the photospheric magnetic field using the PFSS (potential field source surface) model (Schatten, Wilcox, and Ness, 1969; Wang and Sheeley, 1992; Schrijver and De Rosa, 2003). **The back-tracking method typically provides the longitudinal accuracy $\sim 10^0$ at the Sun (**Nolte and Roelof, 1973**). This uncertainty is a result of several reasons including an influence of the solar differential rotation, deviation from the constant solar wind speed condition or deficiency of the coronal magnetic field extrapolation model. The PFSS model is widely used to calculate the magnetic field from the Sun to the source surface but it has weaknesses. In particular, it is not accurate in active regions due to the violation of the current-free assumption and hence will not produce open field lines at the expected locations due to non-simultaneously updated photospheric magnetic maps or unknown evolution of the magnetic field on the hidden far side (**Nitta and De Rosa, 2008**).** Rust *et al.* (2008) **concluded that even if the input magnetic data are updated frequently, the PFSS model only succeed in $\sim$ 50% of cases to identify the coronal segment of open fields.**

The second method which helps to identify the solar wind sources is based on analysis of specific solar wind parameters measured *in situ* **near the Earth such as the solar wind velocity, ionic composition and freezing-in temperature determined from the ionic state distribution. Numerous studies have shown that freezing-in temperature (or corresponding O^{7+}/O^{6+} ratio) and the FIP (first ionization potential) bias have different values for different solar wind sources such as streamers (see e.g.** Raymond *et al.*, 1997**; Strachan** *et al.*, 2002**; Bemporad** *et al.*, 2003**), coronal holes, active regions and their interfaces (**Liewer, Neugebauer, and Zurbuchen, 2004**; Neugebauer** *et al.*, 2002**; Ko** *et al.*, 2006**). Based on comparison of the *ACE* solar wind data with extrapolations of the photospheric magnetic field,** Wang, Ko, and Grappin (2009) **suggested that high O^{7+}/O^{6+} and Fe/O ratios are associated with the slow wind originating from small holes located in and around active regions. The component of the slow wind with intermediate O^{7+}/O^{6+} and Fe/O ratios are likely to originate from the boundaries of large coronal holes (in particular, the polar coronal holes). The high-speed streams in the ecliptic, which originate from interiors of large low-latitude holes and equatorward extensions of the polar holes, are characterized by the lowest O^{7+}/O^{6+} and Fe/O ratios.**

The existence of local sources of the slow solar wind is confirmed by studies of the coronal streamers. By analyzing the motion of small density enhancements in coronal streamers observed with the Large Angle and Spectrometric Coronagraph (LASCO) on the *Solar and Heliospheric Observatory* (*SOHO*), Sheeley *et al.* (1997) **and** Wang *et al.* (1998) **concluded that the major component of the slow wind originates outside the helmet streamers, probably, from the coronal hole boundaries. By applying a tomographic technique to the interplanetary scintillation (IPS) measurements,** Kojima *et al.* (2007) **found that some fine details in the IPS data are produced by compact low-speed streams originated from open field regions in the vicinity of the closed loops.**

Local sources of the solar wind, probably, may be associated with the regions of outflows often detected in the solar corona. Uchida *et al.* (1992) **reported detection of outflows from active regions observed in X-rays as continual expansion of plasma from hot loops.** Švestka *et al.* (1998) **observed fans of transient coronal rays above ARs after flares and suggested that they may contribute to the solar wind. In both cases outflows lasted for periods from several hours to several days.** Winebarger, DeLuca, and Golub (2001) **detected brightness variations along a bundle of coronal loops in the** *TRACE* **171 Å images and interpreted this phenomenon as a signature of outflows with velocities between 5 and 20 km s^{-1}.**

Upflows and downflows were detected in active regions by analysis of the EUV Dopplergrams obtained with the spectrometers CDS (Coronal Diagnostics Spectrometer – Harrison *et al.*, 1997**) and SUMER (Solar Ultraviolet Measurements of Emitted Radiation –** Wilhelm *et al.*,

1997) **onboard the *SOHO* observatory.** Brekke *et al.* (1997) **observed with CDS significant upflows and downflows of plasma in active region loops ("siphon flows"), both at coronal and transition region temperatures reaching velocities of $\sim$50 km s^{-1} and more.** Marsch, Wiegelmann, and Xia (2004) **studied the Doppler shifts of the EUV transition region lines along closed loops in several ARs measured with SUMER in connection with the force-free extrapolation of photospheric magnetic field.**

Since *Hinode* (Kosugi *et al.*, 2007) **was launched, there has been an increasing interest in studying strong upflows (referred to as outflows as it is expected that some of the material leaves the Sun) from the edges of active regions.** Sakao *et al.* (2007) **analyzed a sequence of soft X-ray images taken by the XRT (X-Ray Telescope) telescope** (Golub *et al.*, 2007) **on February 20, 2007 and detected brightness variations in a fan-like structure at the edge of an AR located adjacent to a coronal hole. They interpreted this phenomenon as a signature of continuous outflow of plasma with a temperature of 1.1 MK moving along open magnetic field lines with the velocity of $\sim$100 km s^{-1} and suggested that this outflow was a possible source of the solar wind. Using EIS (EUV Imaging Spectrometer)** (Culhane *et al.*, 2007)**,** Harra *et al.* (2008) **analyzed the FeXII emission line in the same region and found outflow speeds of around 50 km s^{-1}, which after correction for projection effect reached speeds similar to those seen in the XRT imaging data.**

The creation and maintenance of the quasi-stationary outflowing plasma is still being debated. There have been various suggestions as to what could create this outflowing plasma. This includes reconnection over large spatial scales, which is consistent with the low curvature of the fan structure often present in ARs. Harra *et al.* (2008) **showed through magnetic field extrapolation that the edges of the active regions can reconnect with bipoles lying further away from the active region.** Baker *et al.* (2009) **suggested that outflows may originate from specific locations of the magnetic field topology where field lines display strong gradients of magnetic connectivity, namely, quasi-separatrix layers (QSLs). Another option to explain the outflows was put forward by** Murray *et al.* (2010) **who studied the special case of an active region inside a coronal hole. In this case they found through simulations that the outflow could be replicated through the process of compression. Some other mechanisms can produce temporal or quasi-periodic flows: jet or spicule-like events** (McIntosh and De Pontieu, 2009)**, coronal mass ejection providing outflow from dimming region** (Harra *et al.*, 2011)**.**

The outflows detected by the Doppler blue-shifted coronal lines principally could indicate possible source regions of the slow solar wind. The main issue is how to distinguish upflows that actually leave the Sun from that which are just parts of closed "coronal circulation" of the solar plasma (Marsch *et al.*, 2008)**. To solve this question, one needs to analyze the structure of the inner corona between the solar**

surface and the source surface and to identify signatures indicating propagation of outflows to the heliosphere.

The inner corona has not been studied extensively so far. Due to the stray light problem, the existing white-light (WL) coronagraphs typically observe the corona far above the limb (e.g. at the distance of $2.2R_{\rm sun}$ from the solar center in LASCO C2 and C3 coronagraphs (Brueckner *et al.*, 1995), $1.3R_{\rm sun}$ in *STEREO* COR1 coronagraphs (Thompson *et al.*, 2003)), or have too low spatial resolution to resolve its fine structure (Mauna Loa MK4 coronagraph – Burkepile, Darnell, and Tomczyk, 2005). High-resolution pictures of the whole corona taken during total solar eclipses (see e.g. Wang *et al.*, 2007) only show the coronal over a short time interval. Just above active regions the WL corona consists of broad diffuse structures. The contrast enhancing techniques (see e.g. Druckmüller, 2009) do not help much, because their application suppresses diffuse components. Thus, imaging of the corona in the broadband WL cannot be easily used to find the roots of coronal structures at the Sun. An exception is a case of the WL observations in monochromatic spectral lines which will be discussed later.

However, the EUV imaging easily reveals localized coronal structures near the limb, because the stray light in the EUV range is not a problem. Coronal structures observed in the broadband WL and in EUV ranges have significant differences which can be explained by different excitation mechanisms of their radiance. Emission of the K-corona in WL is produced by the Thomson scattering of the solar disk radiation on free electrons, its brightness being proportional to the first order of density. In EUV range, the corona irradiates in spectral lines of ions excited by collisions and by resonant scattering. Close to the Sun the collisional excitation dominates, hence, the brightness of coronal features is proportional to the squared density indicating the strongest magnetic field concentrations. Pasachoff *et al.* (2011) noticed that EUV imaging selects coronal structures with excitation temperatures specific for given spectral lines, whereas the WL streamers include structures irrespective of their temperature.

The first EUV observations of the extended corona in the 175 Å band containing Fe IX–Fe XI lines up to the radial distances $R = 2 - 3R_{\rm sun}$ were carried out with the SPIRIT (SPectrographIc X-Ray Imaging Telescope-spectroheliograph) telescope aboard the *CORONAS-F* (Complex Orbital neaR-Earth ObservatioNs of Activity of the Sun) satellite (Slemzin *et al.*, 2008) at solar maximum of the 23^d cycle. These observations discovered existence of large-scale structures – coronal rays, originated in some active regions and rotated with them to the limb. In the beginning of the 24^{th} solar cycle, in 2009, coronal rays were observed with the TESIS (TElescopic Spectroheligraphic Imaging System telescope in 171 Å band) (Kuzin *et al.*, 2009). Currently coronal rays are systematically observed with the SWAP (Sun Watcher using Active Pixel System detector and imaging processing

telescope) (Berghmans *et al.*, 2006) onboard the *PROBA2* (PRoject for OnBoard Autonomy) satellite in the 174 Å band.

On their periphery, ARs often display fan-like structures which are believed to be partially observed high cool loops. At present, there is no clear understanding about their nature and the relationship with outflows. Schrijver *et al.* (1999) classified fan structures as long lived loops with the temperature of 1 MK fanning out of the *TRACE* field of view. Berghmans *et al.* (1999) reported a detection of propagating disturbances with velocity of the order of 100 km s^{-1} along partially open fan loops observed both in EIT 195 Å and *TRACE* 171 Å images. However, they interpreted this phenomenon as sonic perturbations. Using *SOHO*/CDS, Del Zanna and Mason (2003) have confirmed that the loops seen in the *TRACE* images have temperature of 0.7–1.1 MK. Brooks, Warren, and Young (2011) found that fan loops observed with *Hinode*/EIS and *SDO*/AIA (Advanced Atmospheric Assembly onboard Solar Dynamic Observatory) have peak temperatures in the similar range of 0.8–1.2 MK. On the contrary, Ugarte-Urra, Warren, and Brooks (2009) have analyzed with *Hinode*/EIS brightness variations in different loop populations and suggested that the fan structures visible in *TRACE* 171 Å channel belong to the same population of cool peripheral loops which are prominent in the Si VII and Mg VII 0.6 MK lines and develop downflows with velocities in the range $V \sim 39$–105 km s^{-1}. The authors did not found any evident relation between these fan loops and hotter blueshifted structures which showed transient propagating disturbances seen in the blue wing emission of the Fe XII 195.12 Å line. Warren *et al.* (2011) suggested that the bright fan-like structures seen in colder transition region lines are dominated by downflows in contrast to outflows seen in the emission lines from Fe XI–Fe XV ions. The temperature structure of fan loops and their relation to outflows are still in debate.

A generic relationship between various coronal structures may be established from the analysis of their temperature distributions with the use of the Differential Emission Measure (DEM) method. In a number of recent works the DEM analysis was applied to explore different regions of the Sun observed by the EIS instrument. The temperature structure of quiet Sun (QS) regions was analyzed in the papers by Matsuzaki *et al.* (2007) , Warren and Brooks (2009) and Brooks *et al.* (2009) . In typical quiet regions and active regions Matsuzaki *et al.* (2007) found out a group of loops with temperatures of ∼1 MK and ∼2 MK superposed in the line of sight and the low temperature component at ∼0.4 MK. Warren and Brooks (2009) presented an analysis of temperature and density measurements above the limb in the quiet corona using the EIS data. Brooks *et al.* (2009) carried out a DEM analysis of the quiet solar corona on the disk. For both cases the authors found the plasma temperature component peaked near 1 MK. Landi and Young (2009) reported on a cold, bright portion of an active region observed by the EIS instrument. The emitting region

was characterized by a large maximum at $\log T \approx$ 5.6, corresponding to transition region temperatures, and a broad tail in the DEM distribution extending to higher temperatures. Brooks and Warren (2011) **have studied the outflow regions of AR 10978 and determined, in particular, that the electron density and temperature in the outflows had values of $\log N_e = 8.6$ and $\log T = 6.2$ correspondingly. Summing all cited results, one may conclude that there are several typical temperature components of plasma in outflow regions, fan loops, quiet regions and hotter closed loops, most often dominating at ∼1–1.5 MK.**

The aim of this work is to investigate the probable link between outflows from active regions and coronal structures – fan loops and coronal rays as signatures of the outgoing plasma streams. We consider properties of coronal rays at solar maximum and at solar minimum and indications of their relationship with the solar wind. We examine the relationship between outflows, coronal structures and the slow solar wind for an isolated active region observed with various space solar instruments during a half of the solar rotational period in July–August 2009 at the disk as well as at both limbs. We analyze the EIS intensity and velocity maps, study the temperature structure of the emitting plasma simultaneously in different places using the DEM analysis, and compare coronal signatures of outflows with computed magnetic field configurations. Finally, we consider the possible correlation of the EIS data on outflows with solar wind data measured by PLasma And Supra-Thermal Ion Composition Investigation (PLASTIC) instruments on Solar Terrestrial Relation Observatories (*STEREO*) Behind and Ahead, Solar Wind Experiment Proton and Alpha Monitor (SWEPAM) onboard Advanced Composition Explorer (*ACE*), Solar Wind Experiment (SWE) onboard *WIND* spacecrafts. Summary and conclusions section will resume the results of the study.

2. Coronal rays in the inner corona at solar maximum and minimum

Ordinary EUV telescopes can observe the solar corona only to the distances $R < 1.3-1.5R_{\rm sun}$ due to the limited field of view (FOV) and insufficient sensitivity to exponentially decaying coronal brightness. SPIRIT was the first EUV telescope to have a coronagraphic mode, in which the direct disk radiation was suppressed by using an external occulter which allowed the study of a large part of the inner corona from the solar surface to the radial distance of 2.5–$3R_{\rm sun}$ (Slemzin *et al.*, 2008). The successor of SPIRIT, the TESIS EUV telescope (Kuzin *et al.*, 2009), operated in February–November 2009, also observed the inner corona using a tiltable mirror and wide range of exposure times from tens of seconds to 600 s. Both SPIRIT and TESIS had very low straylight due to their one-mirror Herschel optical design. The SWAP EUV telescope launched on the *PROBA 2* satellite on November 2, 2009 has a design of one-quarter of the EIT telescope with one spectral channel 174 Å (Defise *et al.*, 2007). The telescope is able to observe the whole inner corona in a special "paving" mode, when the satellite tilts the main

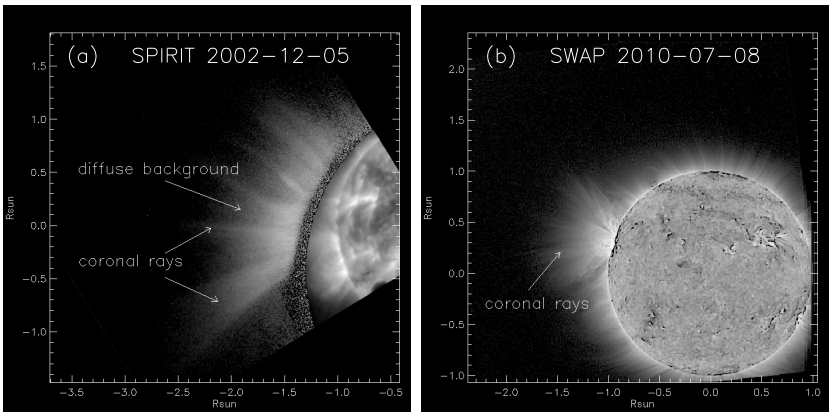

Figure 1. Images of the inner corona: in the SPIRIT 175 Å band (Fe IX – Fe XI lines) taken at solar maximum on December 5, 2002 (a) and in the SWAP 174 Å band (Fe IX – Fe X lines) taken at starting phase of the 24^{th} solar cycle on July 8, 2010 (b). The distances are counted out from the solar center in units of the solar radius.

axis on ∼10 arcmin sequentially in 4 positions (North-East, South-East, North-West and South-West). In each position the telescope takes 80–90 images with a cadence of about 30 s. The images in each paving position are summed and then combined together to obtain a whole image of the inner corona. Typically we see the signal up to $2R_{\rm sun}$ from the disk center. The main limitations are level of straylight and dark current noise.The straylight was extrapolated from radial brightness distribution in periphery regions of the image above $R > 2R_{\rm sun}$ and subtracted.

Figure 1 shows images of the inner corona in the 175 Å band (Fe IX – Fe XI lines) taken by SPIRIT on December 5, 2002 near the maximum of the 23^d solar cycle (a) and by SWAP in the 174 Å band (Fe IX – Fe X lines) on July 8, 2010 at very low solar activity in the beginning of the new 24^{th} cycle (b). The SPIRIT image of the corona at the East limb between latitudes from -30^0 to $+60^0$ displays several isolated bright rays expanding to the distances more than $2.5R_{\rm sun}$ from the solar center. Below $1.5R_{\rm sun}$ the corona contains also a diffuse (non-resolved) part. Most of the rays are narrow quasi-radial structures declined to the North pole except the ray which expands super-radially in the East-South direction with the angular spread of about $\sim 30^0$ and is declined to the South pole. At the distances between 1.5 and $2R_{\rm sun}$ the rays have brightnesses 2–4 times higher than that of the surrounding diffuse corona. The SPIRIT observations (Slemzin *et al.*, 2008) **have shown that coronal rays have origins in active regions and follow them as the Sun rotates.**

The structure of the corona in the SWAP image taken on July 8, 2010 differs from that at the solar maximum. It consists of short (less in length than $0.5R_{\rm sun}$) fine rays uniformly distributed over the limb and a bundle of longer rays (as long as $1.8R_{\rm sun}$) expanding from a single AR at the East limb. The bundle consists of thin threads super-

radially expanding from the AR within the angle $\pm 60^0$ with respect to the local solar surface normal.

It is important to note that images of the corona obtained during eclipses in the monochromatic Fe X 6374 Å and Fe XI 7892 Å lines (Habbal *et al.*, 2007) **displayed similar features as observed by SPIRIT, TESIS and SWAP in the EUV bands. These lines belong to the same Fe IX – Fe XI ions excited at the plasma temperatures of ∼1 MK. In particular, during the eclipses of 2006, 2008 and 2009 images of the corona in the 6374 Å and 7892 Å lines contained structures extending up to the distances of $3R_{\rm sun}$. Meanwhile, such structures were not observed in the Fe XIII 10747 Å and Fe XIV 5903 Å lines which correspond to the hotter plasma with $T > 1.2$ MK. Similar to the EUV images, the authors found, in the red 7892 Å line images, localized intensity enhancements in different parts of the corona at heights ranging from 1.2 to $1.5R_{\rm sun}$ with no counterparts in broad band WL images. The conclusion was that the extended coronal structures observed in the Fe XI visible lines originate from solar sources with electronic temperature of 1.1 MK which agrees with our suggestion based on the imaging of the corona in the EUV spectral band.**

Summarizing the properties of the coronal rays in the inner corona we can conclude that:

- the solar corona sometimes displays bright coronal ray-like structures expanding from the limb up to $R = 2 - 3R_{\rm sun}$;
- at solar maximum coronal rays are seen as numerous, isolated narrow structures, distributed in a wide range of latitudes, whereas at solar minimum they appear as single bundles of thin threads with wide angular spread;
- at distances $R > 1.5R_{\rm sun}$ coronal rays are seen as the brightest and longest in the Fe IX – Fe XI lines excited at temperatures $T \sim 1$ MK in the EUV lines as well as in the visible lines of the same ions, whereas structures in hotter lines, excited at $T > 1.2$ MK mostly corresponding to closed loops are seen only below this radial distance;
- the coronal rays in EUV are well localized above active regions and follow them as the Sun rotates.

Of course, not all coronal rays represent the outflowing plasma streams. Some of them may be lower parts of very large loops invisible in their middle part due to the plasma conditions. The real open structures may be distinguished if they are co-aligned with open magnetic field lines started from the same origin.

3. Case study of the active region in July-August 2009

We investigate the relationship between outflows at the Sun and their coronal signatures by studying an isolated active region observed at the solar disk from July 25 to August 8, 2009. The active region, not numbered by NOAA **(the**

former AR 1024 in the previous rotation), was observed **near the central meridian on July 28 with the** *STEREO-B* **EUVI telescope in the 171 Å band (**Howard *et al.*, 2008**) (see Figure 2 (a) and (b))**. The structure of the AR consisted of a system of loops extended in the direction from South-East to North-West. **Four groups of fan loops f1–f4 were observed in the eastern and western sides of the AR. The fans have lower curvature than the ordinary closed loops in the center of the AR, hence, probably, they are roots of very long loops or even open rays.**

The EUVI telescope on *STEREO-A* **observed the AR near the central meridian in the same band nine days later, on August 6 (Figure 2 (c) and (d)). During the period from July 28 to August 6 the AR structure has appreciably changed. In particular, the closed loops in the AR center were completely disappeared. The fan loops were also evolved: the f1 and f3 groups disappeared, the brightness of f2 increased and a new group f5 appeared in the AR center, probably, in the roots of the former closed loops. It should be noted that on August 6 the fan rays were located near their initial positions in the eastern and western sides of the AR.**

On July 25 the AR was observed at the eastern limb by the TESIS telescope onboard the CORONAS-Photon satellite. Figure 2 (e) and (f) displays two TESIS images taken on July 25 and on August 7, when the AR was located at the eastern limb and near the western limb, respectively. These TESIS images were the closest in time to the above mentioned *STEREO-B* **and** *STEREO-A* **images (between July 28 and August 1, 11:26:40UT TESIS was out of operation). The coronal structure above the AR at the eastern limb contained only closed loops which agreed well with the configuration seen on the *STEREO-B* disk image in Figure 2(a). To August 7 the configuration of the AR changed, and most of the closed loops disappeared. As a result, the corona at the western limb showed coronal rays instead of loops. The rays were not very long, probably, due to the low plasma density in their base.**

The X-ray and EUV instruments *Hinode*/**XRT (**Golub *et al.*, 2007**) and EIS (**Culhane *et al.*, 2007**),** *SOHO*/**EIT (**Delaboudinière *et al.*, 1995**) and** *CORONAS-Photon*/**TESIS (**Kuzin *et al.*, 2009**) observed the AR at the disk close to the central meridian on August 1. Figure 3(a) shows the image of the Sun taken by the** *Hinode*/**XRT on August 1, 06:21:03UT, in the full frame mode. The zoomed area marked by the box in the full frame image with the AR in the center is displayed in the partial frame image (Figure 3(b)). The main solar structures seen in the XRT image are the AR, the polar coronal hole (PCH), the mid-latitude coronal hole northward from the AR (CH1) and a small coronal hole adjacent to the western side of the AR (CH2).**

A sequence of the partial frame images taken by XRT between 00:00 and 08:00 showed a flare peaking at 03:02 UT accompanied with a loop expansion. The light curve of the XRT total intensity in the partial frame from 00:00 to 08:00 UT is shown in Figure 3(c). The *Hinode*/EIS instrument scanned the AR, in a

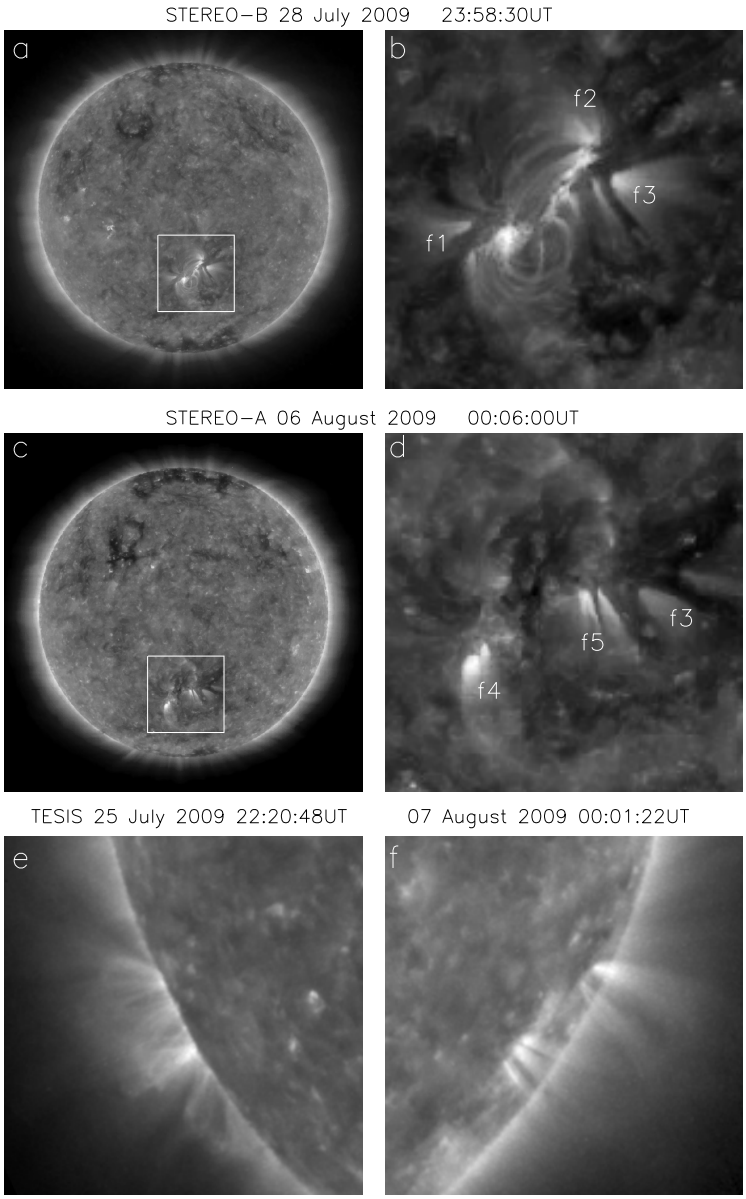

Figure 2. Images of the AR in the 171 Å band taken by: *STEREO-B*/EUVI at the disk on July 28, 2009 (a) with zoomed box around the AR (b), *STEREO-A*/EUVI at the disk on August 7, 2009 (c) with zoomed box (d); *CORONAS-Photon*/TESIS at the eastern limb on July 25 (e) and at the western limb on August 6, 2009 (f). Letters f1-f5 indicate fan loops.

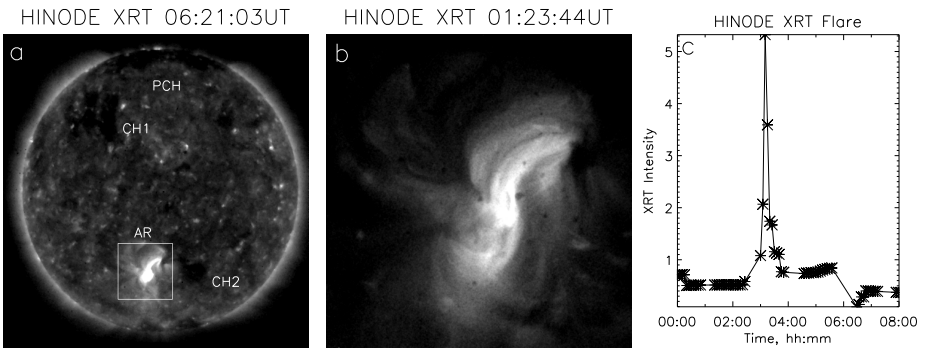

Figure 3. (a)*HINODE*/XRT full frame image taken on August 1, 2009 at 06:21:03UT. The indicated objects are: the AR under study (AR), polar coronal hole (PCH) and two mid-latitude coronal holes (CH1 and CH2). (b) One of the zoomed partial frame images taken at 01:23:44UT. (c) The X-ray light curve measured by XRT in the partial frame containing the AR from 00:00 to 08:00UT showing the flare peaked at 03:02UT.

range of emission lines, from 01:22:14 to 02:57:14 UT. The flare started when the raster reached the left side of the frame and hence the EIS image corresponds to the undisturbed AR structure.

EIT observed the marked region on August 1 in the course of its ordinary 12 min synoptic sequence in the 195 Å band. The EIT images are very useful to make a bridge between the XRT and EIS observations in the beginning of August 1 and the following TESIS observations which started at 11:26:40 UT on August 1 and continued during a week to August 8 when the AR reached the West limb. Figure 4 shows a series of EIT images in 195 Å taken at the beginning of the EIS scan (01:23:17 UT, panel (a)), after maximum of the flare (03:11:34 UT, panel (b)) and near the beginning of the TESIS observations on that day (11:47:17 UT, panel (c)). The panel (d) shows the difference between the images taken at 04:35:17 UT and at 01:23:17 UT with the dimming appearing after the flare in the Eastern part of the AR. At 01:23:17UT (Figure 4(a)) the positions and brightnesses of the fan loops f1–f3 were practically the same as seen on July 28 by *STEREO-B* (Figure 2(b)). After the flare, at 11:47:17UT (Figure 4(c)) the f1 fan was unchanged, the brightnesses of f2 and f3 decreased by ∼10% and a new fan group f4 appeared at the place of the former loops and the dimming seen in Figure 4(d). For further discussion the contours of the outflow regions determined by the EIS in the next section are superimposed on the difference image.

3.1. EIS observations of outflows

We analyzed the AR on August 1, 2009 with data from the EUV Imaging Spectrometer (EIS – Culhane *et al.*, 2007) on the *Hinode* spacecraft . The EIS instrument observes in two wavebands: 170–210 Å and 270–290 Å. It has four slit/slot positions: 1″, 2″, 40″, and 266″. In this paper we will analyze data taken with the 2″ slit and using the fine mirror movement to "raster" and build up an image. The standard calibration was used and the emission lines were fitted with a Gaussian profile in order to measure the intensities and Doppler shifts.

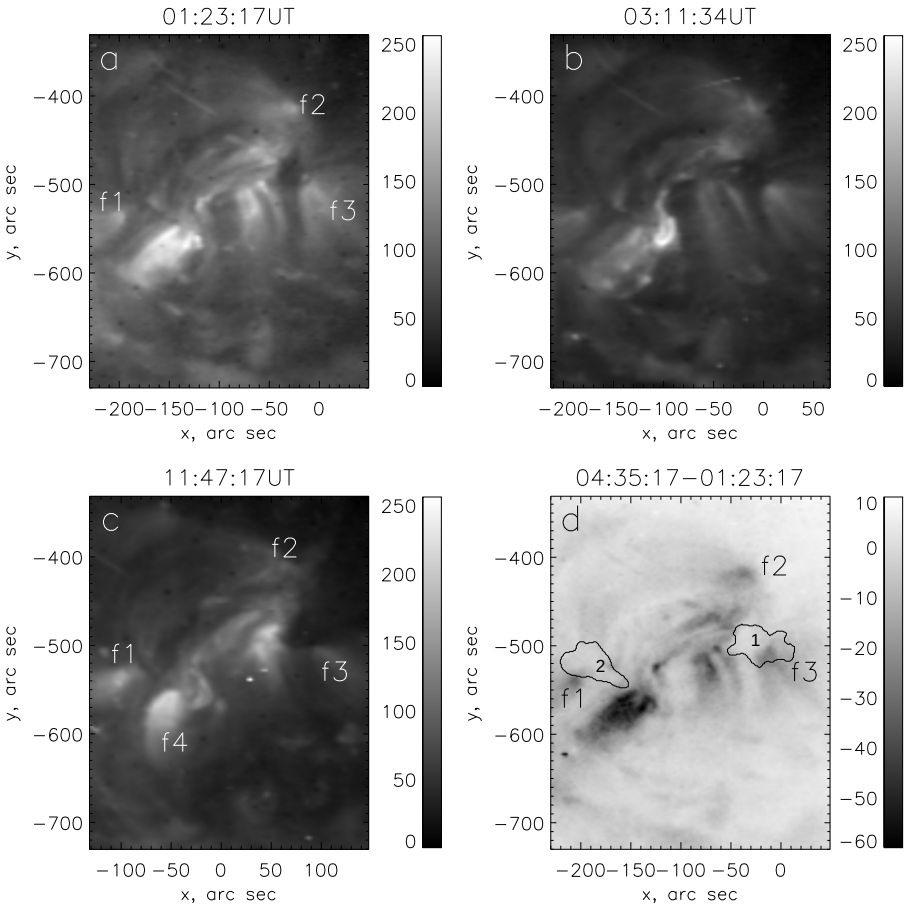

Figure 4. The EIT images in 195 Å taken on August 1, 2009 at the beginning of the EIS scan (01:23:17 UT,(a)), after the maximum of the flare (03:11:34 UT, (b)) and near the beginning of the TESIS observations (11:47:17 UT, (c)), the EIT difference image showing a dimming after the flare at 04:35:17 UT (d). The contours outline regions 1 and 2 correspond to outflows with velocity $|V| > 10$ km s^{-1}determined by EIS from the Doppler shift in the Fe XII emission line (see section 4.1). Letters f1–f4 indicate fan loops determined in Figure 2.

The outflows in active regions have been found to be higher for higher temperature lines as described by Del Zanna (2008) . In order to investigate this dependence in our case, we selected the regions in the Fe XII velocity map where the outflow velocities exceed 10 km s^{-1}. The intensity and Doppler velocity maps are shown in Figure 5 for the Fe X, Fe XII, Fe XIII, Fe XIV and Fe XV lines. The areas of two largest regions in the Fe XII line are contoured and marked by numbers "1" and "2". Region 1 is located at the western boundary of the AR in the interface region with the adjoined coronal hole CH2. Region 2 is located in the eastern side of the AR between bright loops. In all lines emission in both regions is weaker than in the surroundings, but higher than in quiet regions or in the coronal hole CH2.

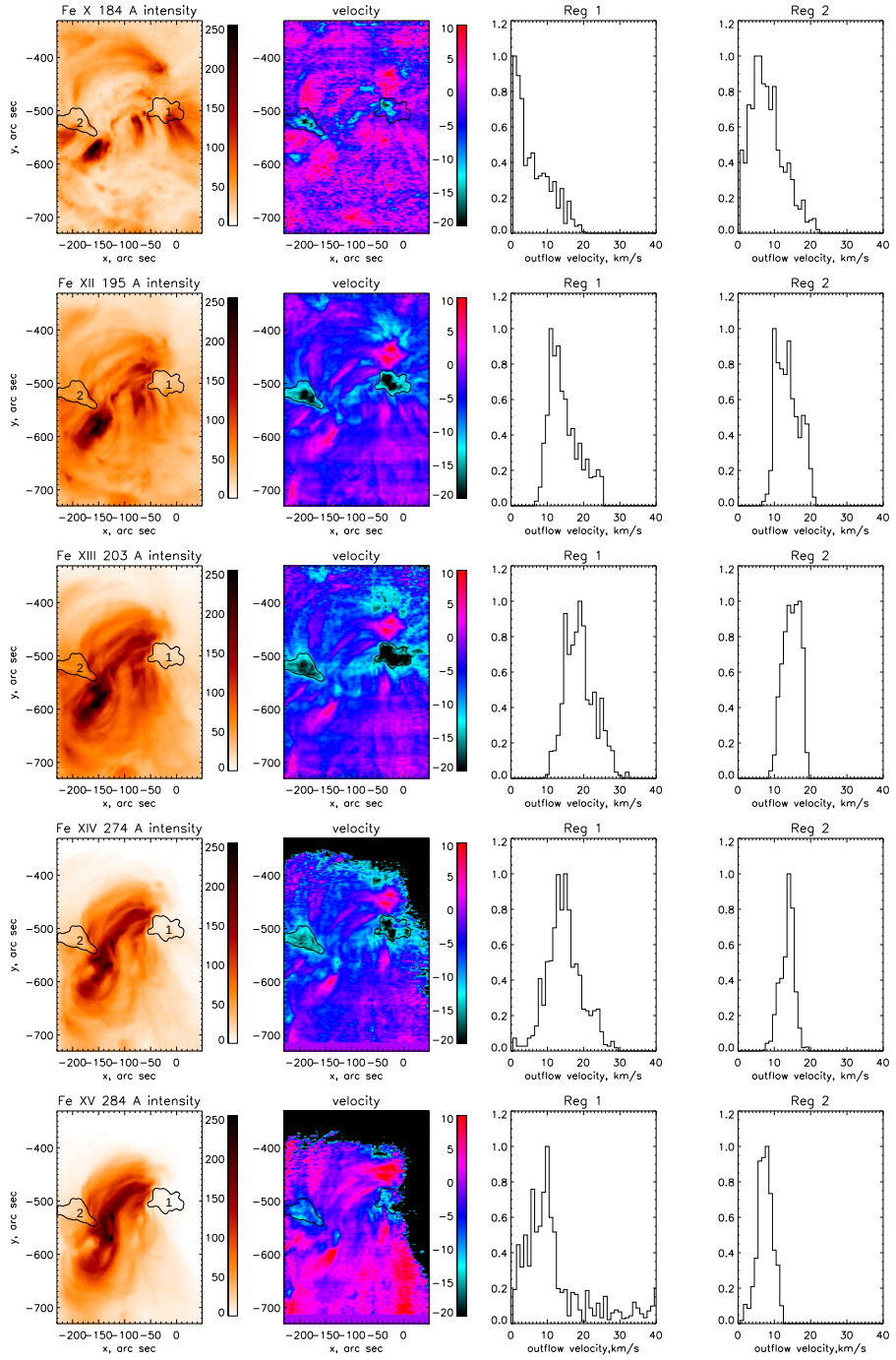

Figure 5. The Fe X, Fe XII, Fe XIII, Fe XIV and Fe XV intensity and Doppler velocity maps for the 1 August 2009 EIS raster. The blue colour shows the upflowing plasma, and the red colour shows the downflowing plasma. The contours correspond to the largest outflow regions defined from the Fe XII velocity map by the condition $|V| > 10$ km s^{-1}. The two right columns demonstrate histograms of the outflow velocity distributions in the regions 1 and 2 for corresponding Fe ions.

The velocity histograms for all ions are shown in the two right columns. The emission becomes weaker as the temperature of the plasma increases, but the Doppler velocity increases from Fe X to Fe XIII and then decreases for Fe XIV and Fe XV. The size of the areas where outflow exceed 10 km s^{-1} follows this dependence. It should be noted that in all cases the highest velocities are concentrated in the central parts of these areas which are spatially correlated in all lines. However, the outflowing velocities are weak, not exceeding 30 km s^{-1} in projection to the line-of-sight. Although the signal statistics for the highest ionized ions Fe XIV and Fe XV in the region 2 is lower than that in the region 1, the principal dependence of velocity on the ionization state is the same for both regions. The fan loops marked by letters f1–f5 in Figures 2, 4 and 5 are most clearly seen in the Fe X emission line.

It should be noted that region 1 crossed the central meridian between July 31, 23UT and August 1, 08UT, region 2 – between August 1, 21UT and August 2, 06UT. We did not observe the AR with EIS after the flare and cannot verify that region 2 remained or disappeared after this evolution and only suggest that the eruption produced the dimming in Figure 4(d) may also contribute to the total outflow when this longitude crossed the central meridian.

We tested the distribution of the line-of-sight velocities across the outflow region 1 and along the fans in different Fe-ion lines. Figure 6 shows the "S-S" scanning line crossing region 1 and adjacent fan loops. The velocity in the Fe X spectral line inside region 1 is negative reaching inside it the maximum of $|V| = 17$ km s^{-1}. In the fan loops it becomes positive indicating downflow with maximal velocity of 5 km s^{-1} and then falls down to zero. The visible length of the scanned fan loop was of ∼40–60 Mm. In the Fe XII – Fe XV lines the velocities are negative along the full scan length reaching the negative values of -20÷-30 km s^{-1} and gradually decreasing to zero in the fan loops. It is worth to note that in all lines the profiles of velocity inside the outflow region look similar reaching the maximum in the center of the region.

Using the EIS data we estimated the mass flux balance in the AR in different Fe ion lines. We define the mass flux density as $n*v$ where n and v are local values of the plasma density and velocity. As a proxy of density n, we used the square root of the line intensity taking into account that the Fe lines in the lower corona are excited by the electron-ion collisions with assumption that the temperature and the ion abundances are constant. Earlier similar approach was used by Marsch, Wiegelmann, and Xia (2004) **. Integration of the bidirectional flux over the EIS FOV in Fe X line gave that the total down-directed flux amounts about 0.7 of the total outgoing flux. In the Fe XII line the same ratio decreased to ∼ 1/7, in the Fe XIII–Fe XIV lines it fell down to 1/20–1/30. It means that in all lines the resulting total flux is directed outwards at least in the boundaries of the EIS FOV.**

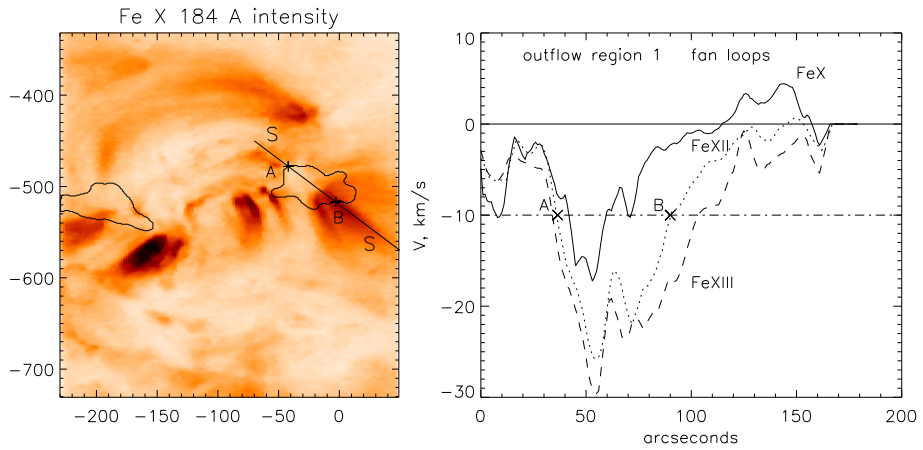

Figure 6. Left panel: the Fe X intensity map with indicated scan line "S-S" across region 1 and adjacent fan loops. The right panel: variations of velocity in the Fe X – Fe XII lines along the scan line. Solid line corresponds to the Fe X velocity, dotted line – to the Fe XII velocity, dashed line – to the Fe XIII velocity. Points A and B designate the boundaries of region 1.

3.2. DEM analysis of plasma temperature distributions

To explore the properties of the outflowing plasma in comparison with other coronal regions, we applied the DEM analysis to different areas in the AR. For that we used the diagnostic technique developed within the framework of the probabilistic approach to the spectral inverse problem for determining the temperature content of the emitting plasma sources (see Urnov *et al.*, 2007**;** Goryaev *et al.*, 2010**). This inversion technique called Bayesian iterative method (BIM) based on the Bayes' theorem is used to reconstruct DEM distributions with the ultimate resolution enhancement (super-resolution) as compared with linear and other non-parametric methods (see** Gelfgat, Kosarev, and Podolyak**,** 1993 **for details, and references therein). The latter property allows the BIM to reconstruct fine temperature structures in the DEM profiles where other DEM techniques derive smoothed and less informative solutions.**

The DEM analysis was applied to the five areas in the AR which are displayed as boxes of 10×10 pixels on the Fe XII velocity map in Figure 7 (left panel). The measured intensity fluxes in EIS spectral lines were obtained using the standard EIS solarsoft. The corresponding EIS lines are listed in Table 1. In this table $T_{\max}$ is the temperature of the maximum abundance for each ion (Mazzotta *et al.*, 1998). To calculate the contribution functions we used the CHIANTI database (version 6.0.1 – Dere *et al.*, 1997; Landi *et al.*, 2006). The DEM analysis was performed adopting the ion fractional abundances of Mazzotta *et al.* (1998) and the coronal elemental abundances of Feldman *et al.* (1992) .

In order to calculate the contribution functions, we also carried out electron density measurements using line ratios. There are a number of density-sensitive

Table 1. List of the EIS lines used in the DEM analysis.

Ion	λ , Å	$\log T_{max}$	Ion	λ , Å	$\log T_{max}$
Fe X	184.54	6.0	Fe XIII	203.83	6.2
Fe XII	186.88	6.1	Fe XIII	203.80	6.2
Fe XI	188.23	6.1	Fe XII	203.72	6.1
Fe XI	188.30	6.1	Fe VIII	186.60	6.0
Fe XII	192.39	6.1	Fe X	257.26	6.0
Fe XI	192.83	6.1	Fe XIV	264.79	6.2
O V	192.90	5.4	Fe XIV	274.20	6.2
Fe XII	195.12	6.1	Si VII	275.35	5.8
Fe XII	195.18	6.1	Fe XV	284.16	6.3
Fe XIII	202.04	6.2	Fe XIV	257.39	6.3

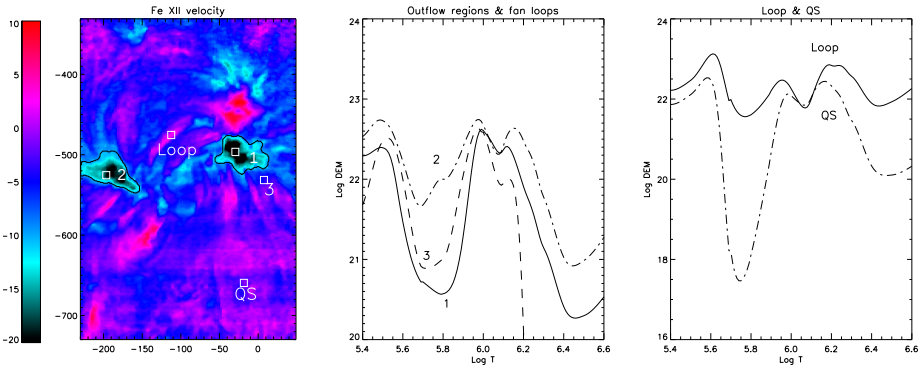

Figure 7. The DEM functions for different solar structures indicated by boxes on the Fe XII velocity map (left panel): 1 and 2 – outflow regions, 3 – fan loops, Loop – closed hot loops, QS – quiet Sun.

line ratios in the EIS wavelength ranges (see, e.g., Young *et al.*, 2009). For the density diagnostics we used the Fe XII $\lambda186.88/\lambda195.12$ ratio sensitive in the range of densities $\log N_e \approx 8$–12 cm^{-3}. The evaluated values of densities for the solar areas under study are found to be $\log N_e \approx 8.4$–9 cm^{-3}.

Figure 7 shows results of the DEM analysis for the solar areas marked by boxes: two outflow regions and fan loops near region 1 (middle panel), closed loop and quiet solar regions (right panel). **In all cases we selected three temperature components in the DEM profiles**: $\log T \sim 5.5$–5.6, $\log T \sim 5.9$–6.0, and $\log T \sim 6.1$–6.2. All the recovered DEM profiles have low temperature components at temperatures of $\log T \approx 5.5$–5.6 (~ 0.4 MK) produced by colder lines of O V and SiVII emitted from the transition region along the line of sight. The high temperature component in closed loops has significantly larger emission measure at $\log T \approx 6.2$ than at temperatures of $\log T \approx 6.0$. The DEM distribution for the QS region demonstrates that the high temperature component at $\log T \approx 6.1$–6.2 exceeds the middle peak at $\log T \approx 5.9$–6.0.

In both outflow regions (middle panel in Figure 7) the plasma contains all three temperature components. The medium temperature component $\log T \approx 6.0$ is the largest indicating that the plasma at temperatures of ≈ 1 MK dominates in the outflow regions. The high temperature component $\log T \approx 6.2$ (≈ 1.5 MK) is less profound than in closed hot loop structures. However, the hotter component is essentially weaker in the fan loops than in the outflow regions. The inferences from our DEM analysis are in particular consistent with the results obtained by Brooks and Warren (2011) who used the Markov Chain Monte Carlo (MCMC) algorithm for the reconstruction of the DEM distributions. Brooks and Warren did not provide the calculated DEM profiles, but the temperatures of the DEM peaks found by these authors for the outflow regions agree with the temperatures obtained in the present work.

3.3. Magnetic field in the AR and evolution of outflows

The photospheric magnetic field map obtained at the Big Bear observatory on August 1, 2009 at 01:22UT is shown in Figure 8 (left panel). The magnetic field in the AR area had a simple dipole configuration being negative at the eastern side and positive at the western side. The left panel shows the magnetic field map in the EIS FOV with superimposed contours of regions 1 and 2. The dashed lines display the boundaries of the outflow regions 1 and 2 determined from the EIS Fe XII velocity map, solid lines – their supposed positions at the photosphere after correction of the projection effect in a simple geometrical model. We assume that the outflowing plasma near the solar surface propagates along the open magnetic field lines directed normally to the solar surface and seen by the observer at the local latitudinal angle -32^0 (the solar coordinates of this area are shown in Figure 13). We compensated the projection effect between the velocity map and the photospheric magnetic map assuming that the Fe XII line is emitted from the height $h \approx 25$ Mm which is a half of the hydrostatic scale of height $H_{\rm hst}$=50 Mm for $T \sim 1$ MK (due to collisional excitation of this line, its intensity is proportional to the density squared, so the intensity scale of height should be equal to 1/2 of its value for density).

The middle and right panels in Figure 8 display the relation between the measured outflow velocities and the line-of-sight magnetic field strength in the regions 1 and 2 projected at the photosphere. According to our model, we consider the radial velocities calculated from their measured line-of-sight values by division on cosine of the angle between the local normal and the line-of-sight. The histograms show distributions of summarized radial velocity versus magnetic field strength. The results show that: (1) outflows emerge from regions of both magnetic field polarities, and (2) the outflow velocities in regions 1 and 2 with $|V| > 10$ km s^{-1} are concentrated at low and medium magnetic fields $|B| \leq 200$ G aside of the regions of the strongest field ($|B|_{\rm max} \approx$ 300–400 G) in the AR. These results differ from the case

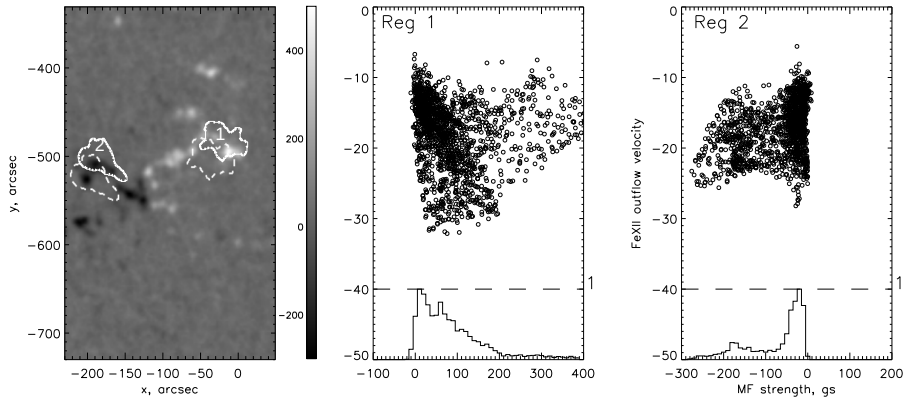

Figure 8. Photospheric magnetic field from the Big Bear observatory data (left panel), and distribution of outflow radial velocities in dependence on magnetic field in the regions 1 (middle) and 2 (right). The dashed contours on the magnetic field map correspond to the outflow regions in the Fe XII line measured by EIS, solid contours – to their positions projected to the photosphere. The graphs in the bottom show the normalized distributions of the total radial velocity flux on magnetic field strength (the scale is in the right axis).

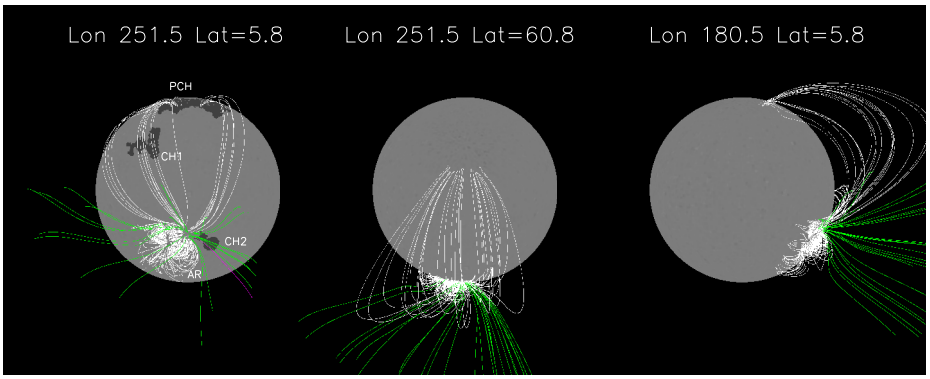

Figure 9. The PFSS extrapolation of the magnetic field in the AR for August 1, 2009, 00:04UT. Closed magnetic field lines are marked by white, open lines (positive) – by green color. PCH – the polar coronal hole, CH1 and CH2 – the mid-latitude coronal holes.

of plasma flows in closed loops studied by Marsch, Wiegelmann, and Xia (2004) **. They found that the outward mass flows corresponded to the strongest fields more than 200 G in the region of negative field polarity while the inward mass flows were associated with positive polarity.**

Figure 9 shows the 3-D map of the coronal magnetic field around the AR on August 1, 2009, 00:04UT. The magnetic field was calculated using the Solarsoft PFSS code *pfss_viewer* based on the *SOHO*/MDI (Michelson Doppler Imager) photospheric synoptic magnetic map with spatial resolution of 1^0. All three pictures display the extrapolated coronal field at different aspect angles: the left picture – as it is seen from the Earth, the middle picture is a top view from the northern

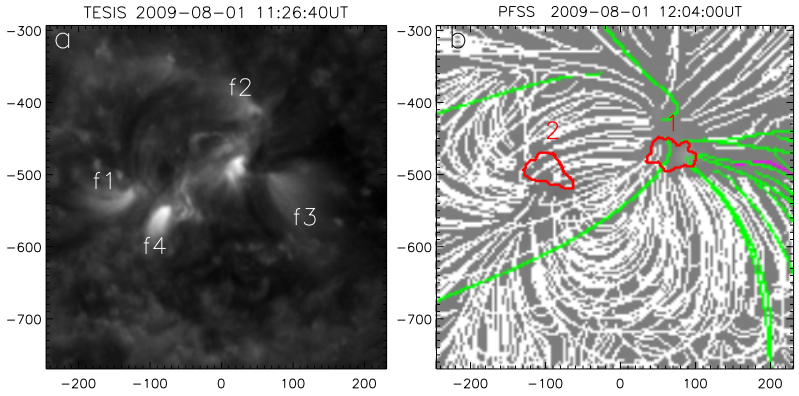

Figure 10. (a) A zoomed image of the AR taken by TESIS in the 171 Å band on August 1 at 11:26:40UT; (b) the magnetic field for the same time obtained with the PFSS extrapolation. Closed magnetic field lines are marked by white color, positive/negative open field lines – by green/magenta color. Red contours show outflow regions projected to the photosphere and differentially rotated to the extrapolation time. The scales are in arc seconds relative to the solar center.

pole, the right picture is a side view from the eastern limb. Two types of field lines are seen in the western part of the AR neighboring to the coronal hole CH2: open field lines with positive polarity and long closed loops ending in the northern polar coronal hole (PCH). There are no field lines connecting the AR with the northward located mid-latitude coronal hole CH1. The top view shows that the bundle of open field lines is expanded within large longitudinal angle. The minor part of lines are declined eastward from the Sun-Earth plane on angles up to 60^0, the majority of lines are declined westward on angles of 5^0–15^0.

Figure 10(a) shows the image of the AR taken by TESIS in the 171 Å band on August 1 at 11:26:40UT. The structure of the AR and positions of the fan loops f1–f4 were similar to that in the EIT image (see Figure 4(a)). Figure 10(b) shows the configuration of the coronal magnetic field extrapolated with the use of the PFSS method. Superimposed are red contours of the outflow regions projected to the photosphere and then rotated from their initial positions at 01:23:14UT to the extrapolation time 12:04:00UT. Closed magnetic field lines are marked by white color, open field lines of positive and negative polarity are marked by green and magenta color respectively. The western region 1 is located in the interface region between the AR and the coronal hole CH2 in the area of negative open field lines. The fan loops f3 go out from this area along open lines in the South-West direction. The fan loops f2, most probably, correspond to a group of long loops connecting the AR with the northward coronal hole CH1 shown in Figure 9. PFSS shows only closed field lines in the area where region 2 and the fan loops f1 and f4 are located. The open configuration of the magnetic field in the western region 1 remained until the AR reached the western limb on August 7.

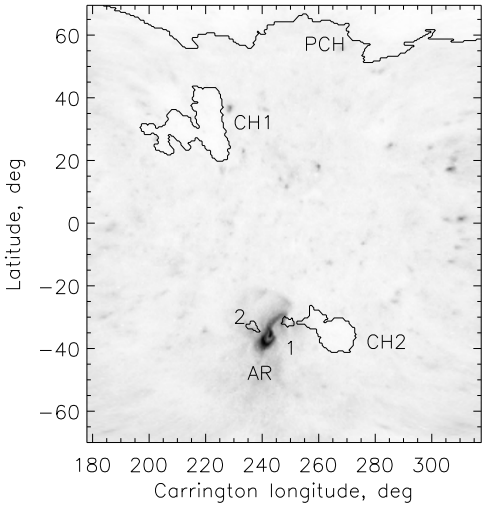

Figure 11. The XRT inverted intensity map in longitude/latitude coordinates (August 1, 2009, 06:21:03UT). Indicated are the EIS outflow regions, the polar coronal hole (PCH) and the mid-latitude coronal holes CH1 and CH2.

4. Analysis of solar wind data and probable imprints of outflows

To identify possible imprints of outflows from the AR to the solar wind near Earth, we analyzed the solar wind parameters measured by instruments on several satellites: by SWEPAM (McComas *et al.*, 1998) **and SWICS** (Gloeckler *et al.*, 1998) **on** *ACE*, **SWE** (Ogilvie *et al.*, 1995) **on** *WIND*, **both rotating around the Lagrangian L1 point, PLASTIC** (Galvin *et al.*, 2008) **on** *STEREO-B* **and** *STEREO-A* **at their orbital positions displaced on some increasing angles from the Sun-Earth line. To compare the solar wind data with the AR structure and outflows measured by EIS, we projected all data to the unified Lon/Lat coordinate plane. Figure 11 shows the XRT solar image taken on August 1 at 06:21:03UT transformed to the Lon/Lat coordinates of the Carrington rotation 2086. Superimposed are the contours of regions 1 and 2 rotated to the time of the XRT image and the contours of the mid-latitude coronal holes CH1 and CH2. The EIS FOV transformed to the Lon/Lat plane lies between longitudes of 233^0 and 254^0, the centers of regions 1 and 2 being at the longitudes 235^0 and 249^0 respectively. The mid-latitude coronal hole CH1 is located at the longitudes 200–230^0, the coronal hole CH2 – at the longitudes 255–265^0.**

To select the solar wind data and to project them to the Lon/Lat coordinates at the source surface, we used the following relation between temporal records of the data and longitudes: $Lon(t) = Lon(t_0) + \varphi + (t_0 - t + \Delta T_b) \times \omega$, **where** $Lon(t_0)$ **is the solar longitude at the reference time** t_0 **(in units of Day of the Year – DOY),** t **the time of data record,**

φ the angle between the spacecraft position in the equatorial plane and the Sun-Earth plane, ω the angular speed of the solar rotation as seen from the spacecraft, and $\Delta T_b = L_{S-S}/V_r$ is the ballistic travelling time, where L_{S-S} is the radial distance between the solar surface at $2.5R_{sun}$ and the spacecraft, V_r the solar wind radial velocity measured at the spacecraft.

For our calculation we used the initial solar longitude $Lon(t_0) =$ **251.5** for the reference time $t_0 = 213.0$ **DOY** seen from the Earth on August 1, 2009 at 00:00UT. For ***ACE*** and ***WIND*** we used $\varphi = 0^0$ and $\omega =$ **13.23** degrees/day, for ***STEREO-A*** $\varphi =$ **57.6**^{0} and $\omega =$ **13.13** degrees/day, for ***STEREO-B*** $\varphi =$ **-49.9**^{0} and $\omega =$ **13.32** degrees/day. All values including distances between the spacecrafts and the source surface were taken at the reference time.

Figure 12 shows the solar wind density (a), velocity (b), O^{7+}/O^{6+} (c) and Fe/O ratios (d) measured by *ACE* as a function of time. All solar wind data are 1h averaged. The graph (e) shows the relation between time and longitudes at the source surface. From this graph it follows that the longitudinal range of the EIS FOV on the source surface **233**^{0}–**254**^{0} corresponds to the ***ACE*** and ***WIND*** data in the time interval between DOY 217.4 and 218.2 (August 5–6) with the mean travelling time 4.5 days. The ***STEREO*** spacecraft observed the same longitudinal range during the time intervals DOY 214.8–215.5 (August 2–3, ***STEREO-B***) and DOY 222–223.4 (August 10–11, ***STEREO-A***). The mean travelling times for those spacecraft were 5.6 and 5.0 days respectively. The projected time intervals at the source surface are July 28–29 (***STEREO-B***), August 1–2 (***ACE/WIND***) and August 5–6 (***STEREO-A***).

A comparison between the solar wind data and the EIS data in the unified longitudinal scale is shown in Figure 13. The panel (a) shows the solar wind (protons) velocity measured by four spacecrafts in three time intervals as a function of longitude. In the longitudinal range **237**^{0}–**260**^{0} the velocities measured by ***ACE*** and ***WIND*** were $V \sim$ **380** km s^{-1}, whereas ***STEREO-B*** and ***STEREO-A*** spacecraft measured lower values of 320–360 km s^{-1}. At longitudes less than **237**^{0} the velocity measured by ***ACE*** and ***WIND*** increased to 480–500 km s^{-1}, whereas ***STEREO-A*** observed a sloping increase and ***STEREO-B*** did not observe any increase at all. We suggest that this increase of the solar wind velocity may be produced by the higher speed wind from the northern coronal hole CH1, although PFSS does not show open field lines starting from there. The difference between velocity of this component measured from various spacecrafts can be explained by evolution of the CH1 during the observational period.

The dependency of the solar wind flux density (a product of density of protons and their velocity $n*v$) on longitude at the source surface are shown in Figure 13(b). The graphs built using the ***ACE*** and ***WIND*** data, which correspond to August 1 at the source surface, are almost identical showing two enhancement features: F1 at **255**^{0} and F2 at

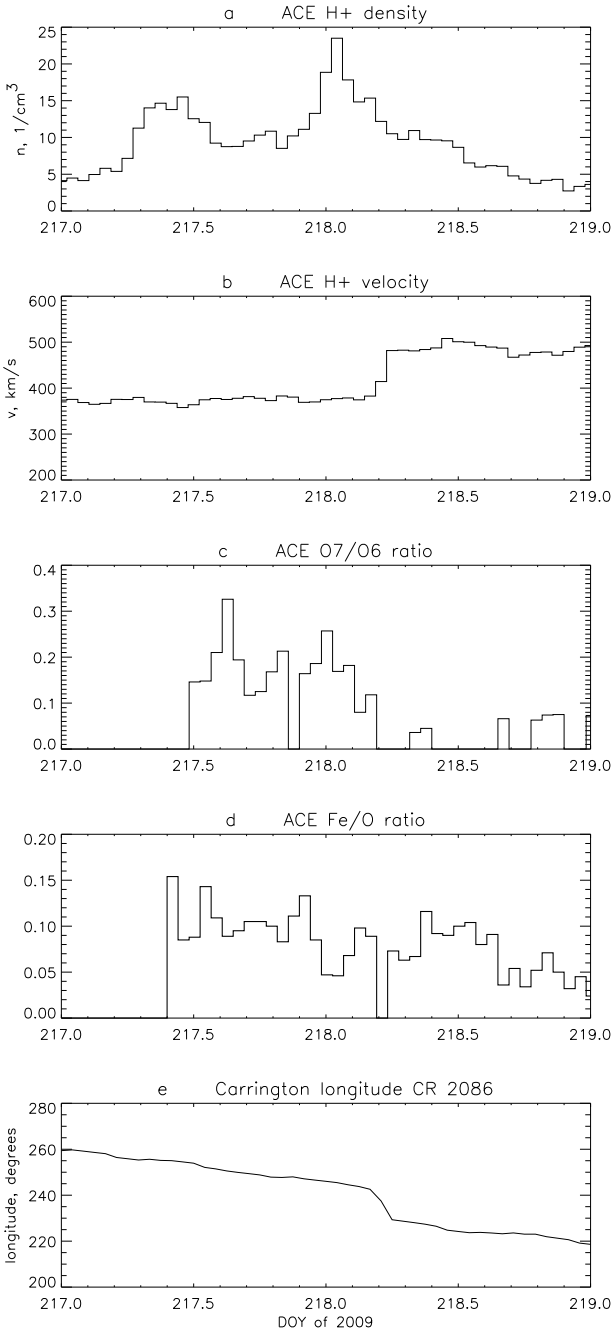

Figure 12. The *ACE* solar wind density (a), velocity (b), O^{7+}/O^{6+} (c) and Fe/O (d) ratios for the period between DOY 217 and 219, 2009 (August 5–7, 2009) and corresponding longitudes at the source surface (e) calculated by means of the ballistic model.

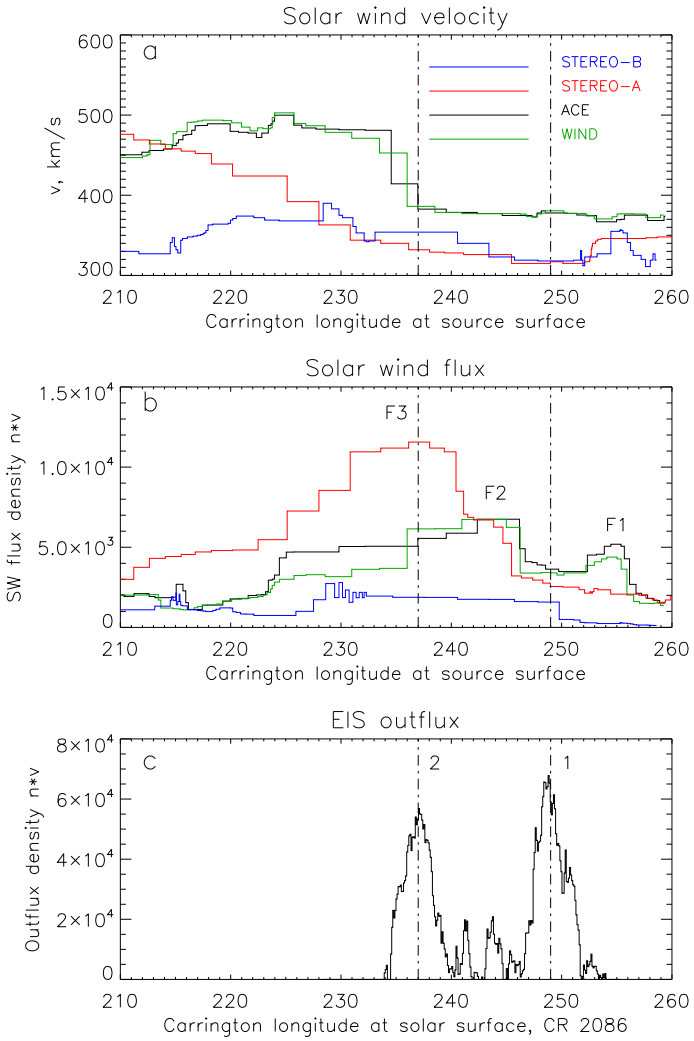

Figure 13. The solar wind velocities (a) and fluxes n∗v (b) determined from the data of *ACE* (black line), *WIND* (green line), *STEREO-B* (red line) and *STEREO-A* (blue line) projected to the Carrington longitudes at the source surface; (c) – the longitudinal distribution of the outflux density determined from the EIS Fe XII data. Vertical lines 1 and 2 correspond to the positions of the outflow regions 1 and 2.

243^0. Four days earlier, the flux density determined from the data of *STEREO-B* was very low without any enhancements. Five days after the ACE/WIND measurements, the flux density from the *STEREO-A* data grew up in two times with the major peak at 237^0 and a weak enhancement on 243^0.

To investigate the probable relationship of these data with the EIS data on outflows, we compared these dependencies with the longitudinal distribution of the outflow flux density $n*v$ (in arbitrary scale)

at the solar surface obtained from the EIS data shown in Figure 13(c). Comparing the graphs on panels (b) and (c), one can notice that the features F1 and F2 in the distribution of the solar wind flux density look similar to the peaks 1 and 2 in the distribution of the outflow flux density shifted towards the West on 6^0. This angle is in agreement with the configuration of the global magnetic field in Figure 9 where open field lines from the AR are declined to the West on 5^0–15^0. We assume that the features 1 and 2 in the *ACE/WIND* graphs could be the required imprints of the outflows from regions 1 and 2 in the solar wind.

The feature F3 in the *STEREO-A* graph coincides with the position of the peak 2 in the EIS graph produced by the outflow region 2. However, the *STEREO-A* solar wind data was obtained five days later than the EIS scan when the AR had noticeably evolved. Although we do not have EIS data during that period, we surmise that the largest feature F3 could be produced by new outflows appearing in the AR as a result of its evolution. It is consistent with the occurrence of coronal rays above the western limb seen by TESIS. In the same way, the density of the solar wind flux determined from the *STEREO-B* data coincided in time with absence of coronal rays at the eastern limb. It is possible that features F2 at the *ACE/WIND* data and F3 at the *STEREO-A* data could contain some contribution from the compression front in the stream interface region between slow and high speed wind from the coronal hole CH1. It should be noted that our comparison is quite qualitative and concerns only longitudinal positions of enhancements in the solar wind and in the outflow. A quantitative relationship between the solar wind and the outflow flux density values can be determined with the help of theoretical modeling which is out of the scope of our study.

Shown in Figure 13 the O^{7+}/O^{6+} ratio measured by *ACE* had the value of 0.17–0.26 in the time interval DOY 217.5–218.2 corresponding to the AR and decreased to $\leq$ 0.05 at DOY 218.2–219 which corresponds to the longitudes of the northern coronal hole CH1. According to Liewer, Neugebauer, and Zurbuchen (2004) **, the first value is typical for the interface region between an AR and coronal hole (in our case CH2). The second low ratio is typical for coronal holes (CH1). The Fe/O ratio averaged over the DOY 217.4–218.2 period is 0.096 and diminishes to $\approx$ 0.07 by DOY 219. According to** Liewer, Neugebauer, and Zurbuchen (2004) **and** von Steiger *et al.* (2000) **, these values agree well with those defined for slow wind from streamer belts and fast wind from coronal holes near solar minimum.**

5. Summary and Conclusions

Summarizing, in the case study of the AR observed at the Sun in the end of July - beginning of August 2009 we have found that:

1. The *STEREO-B*, *STEREO-A* and TESIS data have shown that during the period from July 25 to August 7, 2009 the structure of the AR changed from initially closed to partly open configuration which resulted in appearance of coronal rays detected by TESIS at the western limb. On August 1 EIS revealed two regions of strong outflows in the eastern and western sides of the AR. The western outflow was rooted in the interface region between the AR and adjacent coronal hole (CH2) in which the magnetic field configuration given by PFSS was open. The DEM analysis has shown that the plasma in the outflows and associated fan loops had the same dominating 1 MK component which was responsible for the emission of coronal rays observed by TESIS at the western limb. All these observational results suggest that the coronal rays seen by TESIS at the western limb in ~ 1 MK EUV band are likely represent signatures of outflows from the AR in the inner corona.

2. The fan loops seen in the Fe X line, probably, display downflows at the periphery of the outflow regions whereas the main outgoing flux contains Fe ions in all states from Fe X to Fe XV. It is confirmed by the estimation of the mass flux balance in the lines of different Fe ions. These results agree with the conclusions of Ugarte-Urra, Warren, and Brooks, 2009 **and** Warren *et al.*, 2011**) that fan structures are parts of cool loops indicating downflows, whereas outflows are observed primarily in the Fe XI to Fe XV emission lines.**

3. Analysis of the *STEREO-B* and *STEREO-A* solar wind data projected to the source surface has shown that in the longitude range of the AR the slow wind had velocity of 320-450 km s^{-1}. The solar wind flux density defined as the product of the proton density to their velocity had the minimal value when the configuration of the AR was closed (July 25–28) and the maximal value when the structure became partly opened (August 6–7). The longitudinal distribution of the solar wind flux density at the source surface determined from the *ACE/WIND* data showed similarity with the distribution of the outflow flux density at the Sun defined by EIS shifted westward on 6 degrees. This shift agreed with the magnetic field configuration between the AR and the source surface given by PFSS. The corresponding values of the O^{7+}/O^{6+} and Fe/O ratios were typical for the interface region between AR and CH.

The probable link between the solar wind and the outgoing plasma with the temperature of ~ 1 MK is confirmed by the results of Habbal *et al.*, 2010**. They analyzed the Fe charge distribution in the solar wind measured with the SWICS/*ACE* in 1998 - 2009 and found a peak centered on Fe^{8+}, Fe^{9+} and Fe^{10+} ions. An iterative process based on this distribution and on the Fe ion fraction as a function of electron temperature yields a narrow peak at 1.1 MK. This value well agrees with the dominating component of the plasma temperature in outflows and coronal rays found in our case study.**

However, some questions need further investigation. First, it is not clear, why PFSS shows open magnetic field configuration in region 1 and closed configuration in region 2 although other properties of these regions, except the magnetic field polarity, are similar. There are two possible explanations of this fact. If the extrapolated magnetic field is correct, it means that the outflow from region 2 did not leave the Sun being a part of large scale circulation of the coronal plasma. More likely, the used PFSS method in our case is not accurate or even the potential approximation is not quite suitable to describe the magnetic field topology in ARs. Probably, more reliable results can be obtained with the use of the linear or non-linear force-free magnetic field extrapolation models (see the review of Schrijver *et al.*, 2006**).**

Second, in our case study EIS scanned the AR only once when it was at the solar disk center, whereas the coronal rays were observed at the limb a week later. To obtain a more reliable correspondence between outflows and coronal rays it is necessary to study temporal evolution of outflows during all passage of parent ARs across the disk.

Third, it is likely that the enhancements in the longitudinal distribution of the slow solar wind flux density determined from the data of *STEREO-B*, *ACE*, *WIND*, *STEREO-A*, probably, can be imprints of the outflows from the AR. We did not analyzed here all possible causes which can produce such enhancements so this conclusion is preliminary. The quantitative relationship between local outflows at the Sun and the solar wind can be determined by a detailed MHD modeling with consideration of quasi-stationary plasma flows. The results of our study would provide sufficient starting point for such work.

Acknowledgements We are very grateful to Nariaki Nitta and Andrey Zhukov for useful discussions. Many thanks to anonymous referee for valuable remarks and advises. *Hinode* is a Japanese mission developed and launched by ISAS/JAXA, collaborating with NAOJ as a domestic partner, NASA and STFC (UK) as international partners. Scientific operation of the *Hinode* mission is conducted by the *Hinode* science team organized at ISAS/JAXA. This team mainly consists of scientists from institutes in the partner countries. Support for the post-launch operation is provided by JAXA and NAOJ (Japan), STFC (U.K.), NASA (U.S.A.), ESA, and NSC (Norway). We are grateful to NASA, ESA and the *TRACE* and *STEREO* teams for their open data policy. *SOHO* is a project of international cooperation between ESA and NASA. The *CORONAS-Photon*/TESIS data were provided by the team of the Laboratory of X-ray Astronomy of the Sun of the P.N. Lebedev Physical Institute of Russian Academy of Sciences. We thank the *ACE* SWEPAM and SWICS instrument teams and the *ACE* Science Center for providing the *ACE* data. The WIND SWE experiment is a collaborative effort of Goddard Space Flight Center (GSFC), University of New Hampshire (UNH), and Massachusetts Institute of Technology (MIT). This work was supported by the FP-7 SOTERIA Project of the European Commission and the *PROBA2* Guest Investigation Grant. SWAP is a project of the Centre Spatial de Liege and the Royal Observatory of Belgium funded by the Belgian Federal Science Policy Office (BELSPO). The work was partially supported by the Grant 11-02-01079 of the Russian Foundation for Fundamental Research and the Grant OFN-15 of the Russian Academy of Sciences.

References

Baker, D., van Driel-Gesztelyi, L., Mandrini, C. H., Démoulin, P., and Murray, M. J.: 2009, *Astrophys. J.* **705**, 926.

Bemporad, A., et al.: 2003, *Astrophys. J.* **593**, 1146.

Berghmans, D., Clette, F., et al.: 1999, ESA **SP-448**, 575.

Berghmans, D., Hochedez, J.F., et al.: 2006, *Adv. Space Res.* **38**, 1807.

Brekke, P., *et al.*: 1997, *Solar Phys.* **170**, 163.

Brooks, D.H., et al.: 2009, *Astrophys. J.* **705**, 1522.

Brooks, D.H. and Warren, H.P.: 2011, *Astrophys. J. Lett.* **727**, L13.

Brooks, D.H., Warren, H.P., and Young, P.R.: 2011, *Astrophys. J.* **730:85**, 13pp.

Brueckner, G.E., Howard, R.A., Koomen, M.J., Korendyke, C.M., et al.: 1995, *Solar Phys.* **162**, 357.

Burkepile, J., Darnell, T., and Tomczyk, S.: 2005, AGU abstract SH51C-1220.

Culhane, J.L., et al.: 2007, *Solar Phys.* **243**, 19.

Defise, J.M., Halain, J.P., Berghmans, D. et al.: 2007, Proc. SPIE, **6689**, 66890S-12.

DeForest, C.E.: 2007, *Astrophys. J.* **661**, 532.

Delaboudinière, J.-P., Artzner, G.E., Brunaud, J., Gabriel, A.H., et al.: 1995, *Solar Phys.* **162**, 291.

Del Zanna, G., and Mason, H.E.: 2003, *Astron. Astrophys.* **406**, 1089.

Del Zanna, G.: 2008, *Astron. Astrophys.* **481**, L49.

Dere, K.P., et al.: 1997, *Astron. Astrophys. Suppl.* **125**, 149.

Druckmüller, M.: 2009, *Astrophys. J.* **706**, 1605.

Feldman, U., et al.: 1992, *Astrophys. J. Suppl.* **81**, 387.

Galvin, A.B., Kistler, L.M., Popicki, M.A., Farruga, C.J., Simunac K.D.C, Ellis, L., *et al.*: 2008, *Space Sci. Rev.* **136**, 437.

Gelfgat, V.I., Kosarev, E.L., and Podolyak, E.R.: 1993, *Comp. Phys. Commun.* **74**, 349.

Gloeckler, G., *et al.*: 1998, *Space Sci. Rev.* **86**, 497.

Golub, L., *et al.*: 2007, *Solar Phys.* **243**, 63.

Goryaev, F.F., Parenti, S., Urnov, A.M., Oparin, S.N., Hochedez, J.-F., and Reale, F.: 2010, *Astron. Astrophys.* **523**, A44, 15 pp.

Gosling, J.T., *et al.*: 1995, *Geophys. Res. Lett.* **22**, 3329.

Habbal, S.R., Morgan, H., Johnson, J., *et al.*: 2007, *Astrophys. J.* **663**, 598.

Habbal, S.R., Morgan, H., Druckmüller, M., *et al.*: 2010, *Astrophys. J.* **708**, 1650.

Harra, L.K., *et al.*: 2008, *Astrophys. J.* **676**, L147.

Harra, L.K., Mandrini, C.H., Dasso, S., Gulisano, A.M., Steed, K., and Imada, S.: 2011, *Solar Phys.* **268**, 213.

Harrison, R.A., Fludra, A., Pike, C.D., *et al.*: 1997, *Solar Phys.* **170**, 123.

Hefti, S., Grünwaldt, H., Bochsler, P., and Aellig, M.R.: 2000, *J. Geophys. Res.* **105**, 10527.

Howard, R.A., *et al.*: 2008, *Space Sci. Rev.* **136**, 67.

Ko, Y.K., Raymond, J.C., Zurbuchen, T.H., Riley, P., Raines, J.M., and Strachan, L.: 2006, *Astrophys. J.* **646**, 1275.

Kojima, M., Tokumaru, M, Fujiki, K, Hayashi, K, and Jackson, B.V.: 2007, *Astron. Astrophys. Transactions* **26**, 467.

Kosugi, T., *et al.*: 2007, *Solar Phys.* **243**, 3.

Kuzin, S.V., *et al.*: 2009, *Adv. Space Res.* **43**, 1001.

Landi, E., Del Zanna, G, Young, P.R., Dere, K.P., *et al.*: 2006, *Astrophys. J. Suppl.* **162**, 261.

Landi, E. and Young, P.R.: 2009, *Astrophys. J.* **706**, 1.

Levine, R.H., Altschuler, M.D., Harvey, J.W., and Jackson, B.V.: 1977, *Astrophys. J.* **215**, 636.

Liewer, P.C., *et al.*: 2001, *J. Geophys. Res.* **106**, 15903.

Liewer, P.C., Neugebauer, M., and Zurbuchen, T.: 2003, in M. Velli, R. Bruno, F. Malara (eds.), Solar Wind Ten: Proceedings of the 10-th Int. Solar Wind Conference. AIPCP **679**, p. 51.

Liewer, P.C., Neugebauer, M., and Zurbuchen, T.: 2004, *Solar Phys.* **223**, 209.

Marsch, E., Wiegelmann, T., and Xia, L.D.: 2004, *Astron. Astrophys.* **428**, 629.

Marsch, E., Tian, H., Sun, J., Curdt, W., and Wiegelmann, T.: 2008, *Astrophys. J.* **685**, 1262.

Matsuzaki, K., Hara, H., Watanabe, T., Dere, K.P., Brown, C.M., and Culhane, L.: 2007, *Pub. Astron. Soc. Japan* **59**, S683.

Mazzotta, P., Mazzitelli, G., Colafrancesco, S., and Vittorio, N.: 1998, *Astron. Astrophys. Suppl.* **133**, 403.

McComas, D.J., Bame, S.J., Barker, P., Feldman, W.C., Phillips, J.L., Riley, P., and Griffee, J.W.: 1998, *Space Sci. Rev.* **86**, 563.
McComas, D.J., Goldstein, R., Gosling, J.T., and Skoug, R.M.: 2001, *Space Sci. Rev.* **97**, 99.
McIntosh, S.W. and De Pontieu, B.: 2009, *Astrophys. J. Lett* **706**, L80.
Murray, M.J., Baker, D., van Driel-Gesztelyi, L., and Sun, J.: 2010, *Solar Phys.* **261**, 253.
Neugebauer, M., *et al.*: 1998, *J. Geophys. Res.* **103**, 14587.
Neugebauer, M., Liewer, P.C., Smith, E.J., Skoug, R.M., and Zurbuchen, T.H.: 2002, *J. Geophys. Res.* **107**, SSH 13-1.
Nitta, N.V. and De Rosa, M.L.: 2008, *Astrophys. J.* **673**, L207.
Nolte, J.T. and Roelof, E.C.: 1973, *Solar Phys.* **33**, 241.
Ogilvie, K.W., Chornay, D.J., Fritzenreiter, R.J., Hunsaker, F., Keller, J., Lobell, J., *et al.*: 1995, *Space Sci. Rev.* **71**, 550.
Pasachoff, J.M., Rušin, V., Druckmüllerová, H. *et al.*: 2011, *Astrophys. J.* **734**, 114.
Raymond, J.C., *et al.*: 1997, *Solar Phys.* **175**, 645.
Rust, D.M. *et al.*: 2008, *Astrophys. J.* **687**, 635.
Sakao, T., *et al.*: 2007, *Science* **318**, 1585.
Schatten, K.H., Wilcox, J.M., and Ness, N.F.: 1969, *Solar Phys.* **6**, 442.
Schrijver, C.J., *et al.*: 1999, *Solar Phys.* **187**, 261.
Schrijver, C.J. and De Rosa, M.L.: 2003, *Solar Phys.* **212**, 165.
Schrijver, C.J., De Rosa, M.L. and Metcalf, T.R.: 2006, *Solar Phys.* **235**, 161.
Sheeley, N.R., *et al.*: 1997, *Astrophys. J.* **484**, 472.
Slemzin, V., *et al.*: 2008, *Ann. Geophys.* **26**, 3007.
von Steiger, R., *et al.*: 2000, *J. Geophys. Res.* **105**, 27217.
Strachan, L., Suleiman, R., Panasyuk, A.V., Biesecker, D.A., and Kohl, J.L.: 2002, *Astrophys. J.* **571**, 1008.
Švestka, Z., Fárnik, F., Hudson, H.S., and Hick, P.: 1998, *Solar Phys.* **182**, 179.
Thompson, W.T., Davila, J.M., Fisher, R.R., et al.: 2003, Proc. SPIE, **4853**, 1.
Uchida, Y., *et al.*: 1992, *Pub. Astron. Soc. Japan* **44**, L155.
Ugarte-Urra, I., Warren, H.P., and Brooks, D.H.: 2009, *Astrophys. J.* **695**, 642.
Urnov, A.M., Shestov, S.V., Bogachev, S.A., Goryaev, F.F., Zhitnik, I.A., and Kuzin, S.V.: 2007, *Astron. Lett.* **33**, 396.
Wang, Y.-M. and Sheeley, Jr.N.R.: 1990, *Astrophys. J.* **355**, 726.
Wang, Y.-M. and Sheeley, Jr.N.R.: 1992, *Astrophys. J.* **392**, 310.
Wang, Y.M., *et al.*: 1998, *Astrophys. J.* **498**, L165.
Wang, Y.-M., Biersteker, J.B., Sheeley, N.R.Jr., Koutchmy, S., Mouette, J., and Druckmüller, M.: 2007, *Astrophys. J.* **660**, 882.
Wang, Y.-M., Ko, Y.-K., and Grappin, R.: 2009, *Astrophys. J.* **691**, 760.
Warren, H.P. and Brooks, D.H.: 2009, *Astrophys. J.* **700**, 762.
Warren, H.P., Ugarte-Urra, I., Young, P.R., and Stenborg, G.: 2011, *Astrophys. J.* **727:58**, 5 pp.
Wilhelm, K., *et al.*: 1997, *Solar Phys.* **170**, 75.
Winebarger, A.R., DeLuca, E.E., and Golub, L.: 2001, *Astrophys. J.* **553**, L81.
Young, P.R., Watanabe, T., Hara, H., and Mariska, J.T.: 2009, *Astron. Astrophys.* **495**, 587.
Zhao, L., Zurbuchen, T.H., and Fisk, L.A.: 2009, *Geophys. Res. Lett.* **36**, L14104.